Effects of simulation dimensionality on laser-driven electron acceleration and photon emission in hollow microchannel targets

Tao Wang, David Blackman, Katherine Chin, and Alexey Arefiev
Department of Mechanical and Aerospace Engineering, University of California at San Diego, La Jolla, California 92093, USA and Center for Energy Research, University of California at San Diego, La Jolla, California 92093, USA

(Received 15 April 2021; revised 5 August 2021; accepted 24 September 2021; published 18 October 2021)

Using two-dimensional (2D) and three-dimensional (3D) kinetic simulations, we examine the impact of simulation dimensionality on the laser-driven electron acceleration and the emission of collimated γ-ray beams from hollow microchannel targets. We demonstrate that the dimensionality of the simulations considerably influences the results of electron acceleration and photon generation owing to the variation of laser phase velocity in different geometries. In a 3D simulation with a cylindrical geometry, the acceleration process of electrons terminates early due to the higher phase velocity of the propagating laser fields; in contrast, 2D simulations with planar geometry tend to have prolonged electron acceleration and thus produce much more energetic electrons. The photon beam generated in the 3D setup is found to be more diverged accompanied with a lower conversion efficiency. Our paper concludes that the 2D simulation can qualitatively reproduce the features in 3D simulation, but for quantitative evaluations and reliable predictions to facilitate experiment designs 3D modeling is strongly recommended.

DOI: 10.1103/PhysRevE.104.045206

I. INTRODUCTION

The interaction of high-power ultraintense lasers and structured (both nanostructured [1–7] and microstructured [8–18]) targets has been a topic of great interest for its capability of enhancing the laser energy conversion efficiency [1], high-order harmonics generation [19,20], charged particles (relativistic electrons and ions [3,4,18]) acceleration, and the production of x-ray [1,21–23] to γ-ray [15,16,24] radiation. The produced charged particle and photon beams have a wide range of applications from medical ion therapy [25,26] and nuclear physics [27,28] to photon-photon pair production [29–31]. The microstructured targets with characteristic size of surface modulation comparable to laser wavelength are able to extensively absorb laser energy through various processes, including surface plasmon resonance excitation [32], multipass stochastic heating [33] in dense clusters, prolonged acceleration distance in hollow channels [10] and microwires [11], and relativistic transparency in prefilled channels [15]. In this paper, we examine the regime involving hollow microchannels (see Fig. 1).

When ultraintense lasers irradiate hollow microchannels, strong laser fields directly act on electrons, dragging them into the channel and forming periodic electron bunches which then surf along with the laser pulse, gaining energy from the laser. Additionally, the presence of a channel guides the propagation of the electromagnetic fields, confines the electron motion, and as a result leads to a well collimated photon emission. This setup can serve as a promising electron source to further stimulate ion acceleration [18] as long as the ion expansion does not significantly impact electron acceleration [34]. However, to successfully apply such an electron source in experiments, careful numerical investigations are needed in order to determine where the electron energy peaks, i.e., the location to cut off the channel and collect an electron source with an optimal spectrum.

To carry out such numerical studies, one can choose between 2D3V and 3D3V Particle-In-Cell (PIC) simulations. Both two-dimensional (2D) [8–10,35,36] and three-dimensional (3D) [13,14,17,37,38] numerical simulations have been widely used to characterize laser interactions with structured targets. The appeal of 2D simulations is that they require significantly less computational resources than 3D simulations, so one is able to perform extensive parameter scans using 2D simulations. However, the field topology differs between 2D and 3D setups and it is not immediately clear how the differences impact the particle dynamics. It is then important to evaluate the dimensionality effects on a case-by-case basis. A few publications [5,39–41] have discussed the influences of simulation dimensionality on ion acceleration with various target geometries. But, to our knowledge, nobody has examined and explained the physics of dimensional effects on laser-irradiated hollow microchannel targets.

In this paper, we show that the chosen dimensionality has a considerable effect on electron acceleration and the associated photon emission. First, we provide an analytical solution to a test problem to demonstrate that the dephasing rate between the accelerated electron and laser wavefronts strongly depends on simulation geometry. Later we show numerical evidence to demonstrate that the dephasing rate differs with simulation dimensionality and such a difference is the key reason for the distinguished observation in terms of electron and photon beam generation. Through collectively evaluating generated particles and detailed particle tracking, we show that the

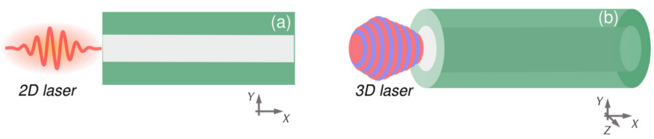

FIG. 1. Laser-irradiated hollow targets in two and three dimensions. (a) 2D setup where a linearly polarized two-dimensional Gaussian pulse interacts with a two-dimensional hollow plasma channel. (b) 3D setup where a linearly polarized and cylindrically symmetric Gaussian pulse interacts with a hollow cylindrical target.

occurrence of high phase velocity in the 3D setup terminates the electron acceleration process early in space and time, and leads to a reduction of photon emission.

II. PHASE VELOCITY IN 2D AND 3D WAVEGUIDES

To provide insights into the role of target geometry on phase velocity, we here consider a simplified waveguide problem with a perfectly conducting boundary. Previous studies [10,34,36] have shown that, in a hollow channel without significant ion expansion, the dominant contributor to electron acceleration is the electric field in the direction of the laser propagation, i.e., the longitudinal field E_x. The corresponding structure of propagating electromagnetic fields can be characterized as TM (transverse magnetic) modes. The wave equation of TM modes can be written as

$$\left(\frac{\partial^2}{\partial y^2}+\frac{\partial^2}{\partial z^2}\right)E_x+\left(\frac{\omega^2}{c^2}-k^2\right)E_x=0, \tag{1}$$

where ω is the wave frequency, k is the wave number, and c is the speed of light. For a two-dimensional waveguide [shown in Fig. 1(a)], E_x is a function of y and $\partial E_x/\partial z=0$. Equation (1) then becomes $\partial^2 E_x/\partial y^2+(\omega^2/c^2-k^2)E_x=0$. We choose $E_x=E_0\sin(\pi y/R)$ as the TM-mode solution that matches the field structure in the incoming pulse (i.e., $E_x=0$ on axis) and the boundary conditions, which requires $E_x(y=\pm R)=0$. Here R represents the radius of the plasma channel. The dispersion equation in the 2D waveguide is then given by

$$\frac{\omega^2}{c^2}=k^2+\frac{\pi^2}{R^2}. \tag{2}$$

For the 3D cylindrical waveguide [shown in Fig. 1(b)], it is convenient to rewrite Eq. (1) in cylindrical form as

$$\frac{1}{r}\frac{\partial}{\partial r}\left(r\frac{\partial E_x}{\partial r}\right)+\frac{1}{r^2}\frac{\partial^2 E_x}{\partial\psi^2}+\left(\frac{\omega^2}{c^2}-k^2\right)E_x=0, \tag{3}$$

where r is the axial distance and ψ is the azimuth. Assuming a solution in the form of $E_x=f\sin(\psi)$, the resulting equation for f then reads

$$s^2\frac{\partial^2 f}{\partial s^2}+s\frac{\partial f}{\partial s}+(s^2-1)=f. \tag{4}$$

Here $s\equiv\beta r$ and $\beta^2=\omega^2/c^2-k^2$. The solution for f is given by $f=E_\parallel J_1(s)=E_\parallel J_1(\beta r)$ where $J_1(x)$ is a Bessel function of the first kind and $E_\parallel$ is the amplitude of the longitudinal field. At the boundary of the cylindrical waveguide, $f(r=R)=0$, which yields $\beta R\approx 3.8$. The dispersion relation of the 3D cylindrical waveguide is then written as

$$\frac{\omega^2}{c^2}=k^2+\frac{14.7}{R^2}. \tag{5}$$

It is convenient to derive a general expression for $v_{\rm ph}$ of a propagating wave with the dispersion relations given in Eqs. (2) and (5):

$$u=\frac{v_{\rm ph}}{c}=\frac{\omega}{kc}=\sqrt{1+\frac{\alpha^2}{R^2k^2}}\approx\sqrt{1+\frac{\alpha^2}{R^2k_0^2}}, \tag{6}$$

where we set $k\approx k_0=\omega/c$, $\alpha^2=\pi^2\approx 9.9$ for the 2D channel and $\alpha^2=14.7$ for the 3D cylindrical channel. Subtracting the $v_{\rm ph}$ from c, in the limit of $\alpha^2\ll R^2k_0^2$ we have

$$\delta u=u-1\approx\frac{1}{2}\frac{\alpha^2}{R^2k_0^2}. \tag{7}$$

δu is a dimensionless parameter used to quantify the degree of superluminosity [42]; it can be understood as a dephasing rate, since it illustrates how quickly the local laser wavefront outpaces the electron in question. The ratio of the dephasing rate for the case in two dimensions to that in three dimensions is

$$\frac{\delta u_{\rm 3D}}{\delta u_{\rm 2D}}\approx 1.5. \tag{8}$$

It is worth pointing out that Eqs. (7) and (8) are built on simplified boundary conditions and the neglect of the influence of extracted electrons, thus one may find discrepancies in phase velocity when compared to self-consistent PIC simulations. Nevertheless the difference of dephasing rate in Eq. (8) motivates us to investigate the role of target geometry on phase velocity with numerical simulations. In the following sections we are going to demonstrate via PIC simulations that the laser phase velocity varies with the dimensionality of the simulations and the lower dephasing rate in two dimensions leads to an overestimate of electron acceleration and γ-ray emission.

III. IMPACT OF DIMENSIONALITY ON ELECTRON ACCELERATION

We model the electron acceleration through fully relativistic PIC simulations using the EPOCH code [43], which is available in both two and three dimensions. The target geometries implemented in the simulations are depicted in Fig. 1. In two dimensions, the target is a straight empty channel enclosed by two uniform plasma slabs. In three dimensions, the channel is enclosed by a cylindrical wall of plasma, with a channel diameter such that a slice along the target axis would be identical to the 2D setup. The 2D and 3D simulations share the same plasma composition, plasma density, laser intensity, temporal profile, and laser spot size. The laser intensity is set as 1.37×10^{22} W/cm^2, corresponding to $a_0=100$. Here $a_0\equiv|e|E_0/(m_e c\omega)$ is the normalized laser amplitude, where E_0 is the peak amplitude of the electric field in the incoming laser pulse, and m_e and e are the electron mass and charge. The laser pulse is always focused at the channel entrance. We choose gold as the original target material with a density of 1.5 g/cm^3. According to the field ionization model, the considered laser pulse is capable of ionizing gold atoms to the

TABLE I. Parameters used in 2D and 3D PIC simulations.

Parameters shared by 2D and 3D simulations	
Laser pulse	
Peak intensity	1.37×10^{22} W/cm^2
a_0	100
Polarization	Linearly along $\hat{\mathbf{y}}$
Wavelength	$\lambda_L = 1$ µm
Location of the focal plane	$x = 0$ µm, surface of plasma
Pulse temporal profile	Gaussian
Pulse duration (FWHM for intensity)	30 fs
Pulse width/focal spot (FWHM for intensity)	$w_0 = 2.8$ µm
Plasma	
Composition	Gold ions and electrons
Channel radius	$R = 4.0$ µm
Target thickness	$d = 0.4$ µm
Electron density	$n_e = 276 n_{\rm cr}$
Ion mass to charge ratio	$197 m_p : 69$
Ion mobility	Mobile
Parameters varying in 2D and 3D simulations	
Spatial resolution	2D: 100/µm × 100/µm
	3D: 50/µm × 50/µm × 50/µm
No. of macroparticles/cell	2D: 100 for e^-, 5 for Au^{+69}
	3D: 10 for e^-, 5 for Au^{+69}
Laser geometry	2D: symmetric about y-axis
	3D: cylindrical symmetry
Laser power	2D: 0.82 PW[a]
	3D: 1.24 PW
Target length	2D: $L = 350$ µm
	3D: $L = 150$µm

[a]To calculate the laser power, we assume the length of the third dimension in 2D simulations as 2 µm.

level of $Z = 69$. In the simulations, the target is preionized accordingly to a plasma composed of Au^{+69} (density 4 $n_{\rm cr}$) and e^- (density 276 $n_{\rm cr}$) where $n_{\rm cr} \equiv m_e\omega/(4\pi e^2)$ is the critical density. A detailed comparison of parameters used in the 2D and 3D simulations is listed in Table I. Note that although the target lengths are set differently, this is done such that in different dimensionalities the target is long enough for the electrons to reach their first energy peak.

Figures 2(a) and 2(b) illustrate the time history of the electron energy spectrum observed in both 2D and 3D simulations. There exists more than one energy peak in both Figs. 2(a) and 2(b) and our focus is on the first energy peak which happens before any deceleration takes effect. It is clear that the maximum electron energy gain achieved in two dimensions significantly exceeds the gain observed in the 3D case. In fact, the first energy peak in two dimensions occurs at $t = 500$ fs with $\varepsilon_e = 1920$ MeV while in three dimensions the peak occurs at $t = 255$ fs with $\varepsilon_e = 1240$ MeV. Figure 2(c) gives a direct comparison of the peak spectra observed in the 2D and 3D simulations. In order to facilitate a comparison between the two simulations, we added a gray star to Fig. 2(a) that represents the energy and time of the first peak from Fig. 2(b). Evidently, the acceleration in two dimensions lasts longer, which results in a more energetic electron spectrum. Note that to make a quantitative comparison with the 3D simulations, we assume a uniform third dimension with a length of 2 µm for the 2D simulation.

To further understand the electron acceleration process, we tracked energetic electrons in both simulations. Figures 2(d) and 2(e) illustrate the trajectories of representative electrons selected from both the 2D and 3D simulations. Plotted in the space of the transverse location (y or r) and time, the trajectories are in agreement with the time history of the electron spectrum given in Figs. 2(a) and 2(b); the electron energies peak at the corresponding moments. Regardless of the dimensionality, the electrons surf along the channel wall while getting accelerated by longitudinal electric fields until reaching their first energy peak. However, the horizontal surfing of electrons in the 3D simulation terminates earlier due to its higher dephasing rate, which will be elaborated in the next section. It is worth noting that the second energy peak observed in Figs. 2(a) and 2(b) is correlated with the electron motion of crossing the central axis, indicating an involvement of the transverse electric field in electron acceleration.

Through evaluating the electron energy spectrum and tracking individual electron motion, we have shown that the dimensionality of simulations significantly impacts electron acceleration. The 2D simulations tend to extend the electron acceleration process, leading to an overestimate of the maximum electron energy when compared to more realistic 3D simulations.

IV. ELECTRIC FIELD PROFILES AND PHASE VELOCITY

An electron traveling in the laser fields gains energy only while staying in the accelerating phase of the electric field. The electron can gain energy from both longitudinal ($E_\parallel = E_x$) and transverse ($E_\perp = E_y,\ E_z$) electric fields. The total work done by the electric fields on a given electron can be expressed as

$$W_{\rm tot} = W_\parallel + W_\perp = -|e|\int_{-\infty}^{t} (E_\parallel v_\parallel + E_\perp v_\perp)\,dt'. \qquad (9)$$

Figure 3 shows the contributions of $W_\parallel$ and $W_{\rm tot}$ to electron relativistic energy at the first peak by binning all electrons according to their energies. In the 2D simulation 95% of the energy of energetic electrons ($\varepsilon_e > 500$ MeV) comes from the work done by the longitudinal electric fields and in the 3D case the quantity is 86%. It is then reasonable to approximate

$$W_{\rm tot} \approx W_\parallel = -|e|\int_{-\infty}^{t} E_\parallel v_\parallel\,dt'. \qquad (10)$$

This simply allows us to narrow down the investigation of electron acceleration to a single component of the electric fields.

At ultrahigh laser intensities, the dephasing rate δu is approximately $(v_{\rm ph} - c)/c$, since for a relativistic electron copropagating with a laser $c - v_x \ll v_{\rm ph} - c$. Figures 4(a) and 4(b) describe the temporal profiles of the transverse electric fields E_y recorded in a moving window. Note that E_y and E_x share the same wave mode and phase velocity. By tracking a fixed field segment, we find that $v_{\rm ph} \approx 1.0031\ c$ in the 2D simulation, and $v_{\rm ph} \approx 1.0063\ c$ in the 3D simulation. The

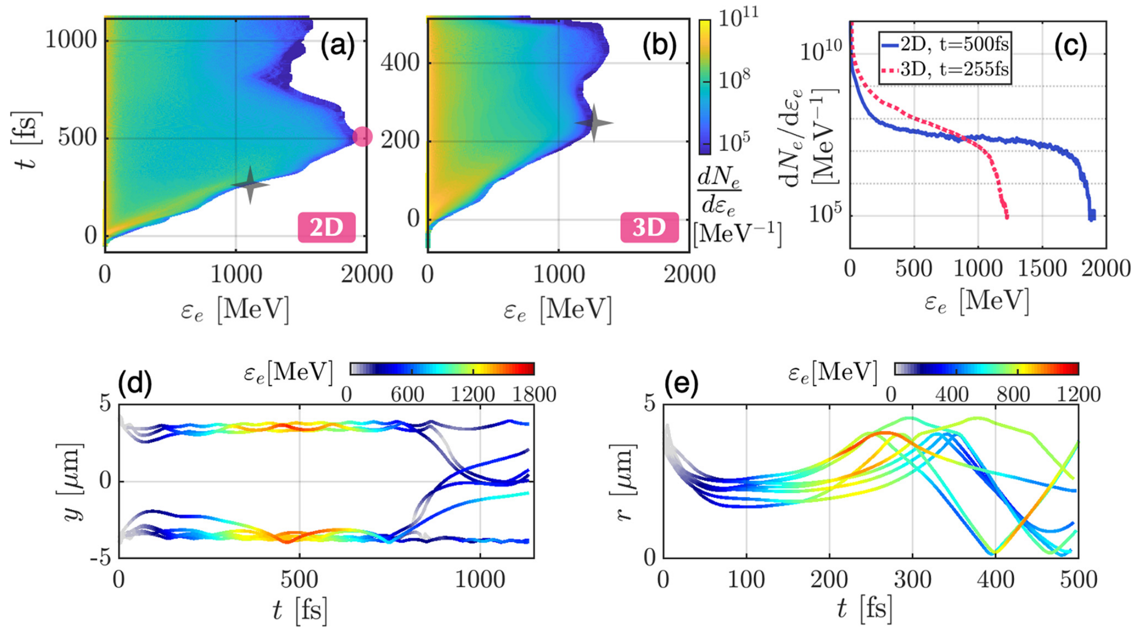

FIG. 2. Time-resolved electron energy spectrum observed in (a) the 2D simulation and (b) the 3D simulation. The colorbar represents the number of electrons collected onto a certain energy bin dε_e. (c) The peak energy spectrum in two and three dimensions which occurred at $t = 500$ fs (marked with red circle) and $t = 255$ fs (marked with gray star), respectively. We define $t = 0$ fs as the time when the laser pulse reaches its peak amplitude in the focal plane at $x = 0$ μm in the absence of the target. Typical electron trajectories are plotted in (d) y-t space for the 2D simulation and (e) r-t space for the 3D simulation. Here $r = \sqrt{y^2 + z^2}$. The color on the trajectories represents electron relativistic energy.

dephasing rate in two dimensions is nearly two times lower than that in three dimensions, explaining the distinction between the electron energy gain seen in the two simulations. The duration for electrons staying in an accelerating phase of electric fields can be estimated by

$$\delta t \approx 0.5\lambda_L/(\delta u c), \tag{11}$$

where $0.5\lambda_L$ is the width of the accelerating phase. We find that $\delta t \approx 540$ and 260 fs in two and three dimensions, matching well with the times found from the simulations, demonstrating the accuracy of the approximation used to calculate the phase velocity. The previously derived Eq. (7) however gives the analytical values of the phase velocity as

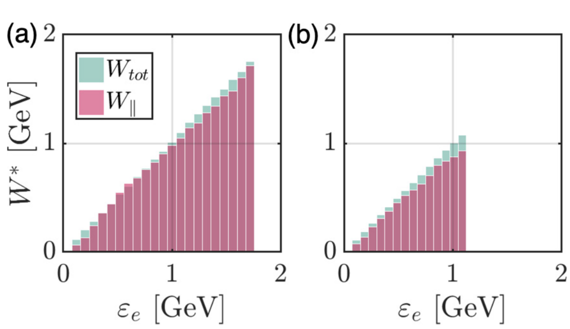

FIG. 3. Contributions to the electron relativistic energy by $E_\parallel$ ($W_\parallel$, red bars) and the electric fields (including both $E_\parallel$ and $E_\perp$, $W_{\rm tot}$, green bars) in (a) the 2D simulation and (b) the 3D simulation. The snapshots are taken at $t = 500$ and 255 fs, respectively, corresponding to the first peak of electron energy spectra in Fig. 2. The bar width in (a) and (b) is set as 75 MeV.

$v_{\rm ph} = 1.0078$ c in two dimensions, and $v_{\rm ph} \approx 1.0116$ c in three dimensions. Despite the difference in numerical value, the same trend of an increase in phase velocity is consistent in both the analytical treatment and the numerical simulations. There are a number of factors that can lead to this discrepancy between the analytical calculations and the numerical simulations, for example, the analytical calculation assumes a perfectly conducting boundary and so requires the transverse fields to be zero at the channel edges [36]; sinusoidal waves are not a perfect match (though close) for the fields observed in the hollow channels; we have neglected the influence of the extracted electrons and their heating [44] on phase velocity. Our additional simulations with different target size R show that as phase velocity varies with R the ratio of δu in two dimensions to δu in three dimensions is preserved. It is worth pointing out that the modification on the dephasing rate brought by the numerical artifacts from the field solver [45] in our PIC simulations is about two orders lower than the values we mentioned above.

To further check how the phase velocity influences electron acceleration, we track representative electrons with respect to E_x fields sampled by them, as illustrated in Figs. 4(c) and 4(d). It is clear that the electrons remain accelerated when they stay in the favorable phase of E_x fields (the negative fields colored in blue). After exiting the accelerating phase, the electron energy declines. As can be seen from the time scale in Figs. 4(c) and 4(d) electrons in the 2D simulation are subject to far longer periods of acceleration than those in three dimensions, due to the lower phase velocity in two dimensions. The evolution of energy and longitudinal work of the chosen electrons is shown in Fig. 4(e). At early moments (up to $\approx$260 fs), the curves of $W_{\parallel\,{\rm 2D}}$ and $W_{\parallel\,{\rm 3D}}$ almost overlap with

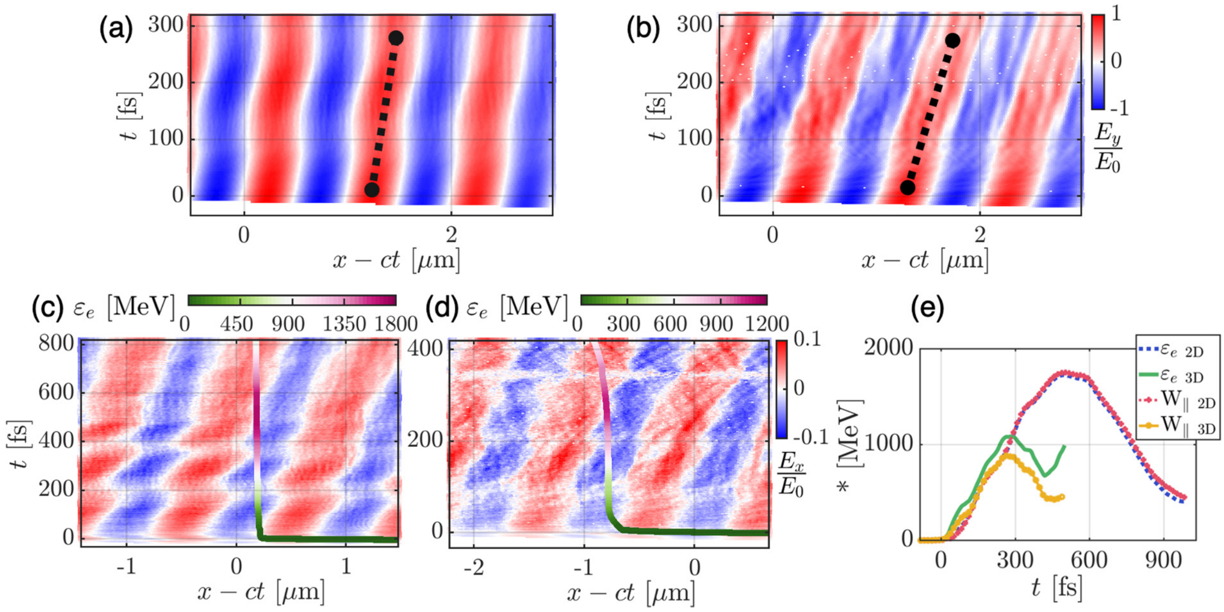

FIG. 4. (a) Temporal profiles of E_y fields on the central axis in (a) the 2D simulation (recorded at $y = 0$) and (b) the 3D simulation (recorded at $y = z = 0$). The E_y fields are plotted in a moving window which moves with the speed of light. Here E_0 with a value of 3.2×10^{14} V/m is the peak amplitude of the electric field in the incoming laser pulse. The black dashed lines show the segments used to determine v_{ph} in each run. The trajectory of a typical high-energy electron is plotted together with the exact E_x fields sampled by that electron in (c) the 2D simulation and (d) the 3D simulation. (e) The comparison of relativistic electron energy and the longitudinal work between the electrons tracked in (c) and (d).

each other, implying that the amplitudes of accelerating fields in two and three dimensions are similar. It is then clear that the major cause for the smaller electron energy observed in the 3D simulation is the early termination of the acceleration process due to the higher dephasing rate. We note in Fig. 4(c) that, although the mean phase velocity is superluminal, for short time intervals (such as $t = 190$–220 fs) the phase velocity becomes subluminal. As shown in the Appendix B, this feature might be explained by the superposition of the fundamental TM mode (the one considered in Sec. II) with higher modes.

So far we used the same channel radius in 2D and 3D simulations, making sure that a slice along the axis of the target in the 3D simulation is identical to the 2D setup. Since the phase velocity varies with the channel radius, one may wonder whether a 2D simulation with a reduced channel radius can match the electron acceleration regime in the 3D simulation. Such a comparison that exclusively focuses on matching the phase velocity overlooks the fact that the electron acceleration depends on two factors: (1) the magnitude of the longitudinal electric field and (2) the time that the electron spends accelerating, which is determined by the phase velocity. By adjusting the channel radius in a 2D simulation, we not only change the phase velocity, but also the amplitude of the accelerating field. This makes it impossible to match the acceleration regime in two dimensions to that in three dimensions via the change in radius.

In order to elaborate on this, we carried out 2D simulations with different channel radii ($R = 2.0$, 3.28, 4.0, and 6.0 μm) while keeping the laser peak intensity and pulse duration constant. We use $R = 3.28\ \mu$m because, according to Eq. (7), the phase velocity at this radius is equal to the phase velocity in the 3D channel. We found that the dephasing rate indeed increases as the channel radius is reduced. For example, as R is reduced from 6.0 to 3.28 to 2.0 μm, δu increases from 7×10^{-4} to 5.1×10^{-3} to 1.27×10^{-2}. However, the reduction of the channel radius significantly changes the amplitude and slope of the accelerating field E_x. The field lineouts are shown in Fig. 7 of Appendix A. Therefore, the adjustment of R makes it impossible to match both factors that determine the acceleration regime, i.e., δu and the field structure of E_x.

V. INFLUENCE OF DIMENSIONALITY ON PHOTON EMISSION

The focus of the discussion in the previous sections was the impact of simulation dimensionality on the laser-driven electron acceleration and generation of energetic electrons with energies of hundreds of MeV to a few GeV. These high-energy electrons are subject to emitting energetic photons (in x-ray and even up to the γ-ray range) while accelerating in laser and channel fields. In this section, we investigate how the photon emission changes with the dimensionality of simulations. The emitted power P_γ of synchrotron emission is determined by the electron acceleration in an instantaneous rest frame. This acceleration is proportional to a dimensionless parameter [46] η:

$$\eta \equiv \frac{\gamma_e}{E_S}\sqrt{\left(\mathbf{E} + \frac{1}{c}[v \times B]\right)^2 - \frac{1}{c^2}(E \cdot v)^2}, \qquad (12)$$

where $\mathbf{E}$ and $\mathbf{B}$ are the electric and magnetic fields acting on the electron, γ_e and $\mathbf{v}$ are the relativistic factor and the velocity of the electron, and $E_S \approx 1.3\times10^{18}$ V/m is the Schwinger field. The emitted power from an electron scales as $P_\gamma \propto \eta^2$. We are interested in photons with energy above 100 keV, a

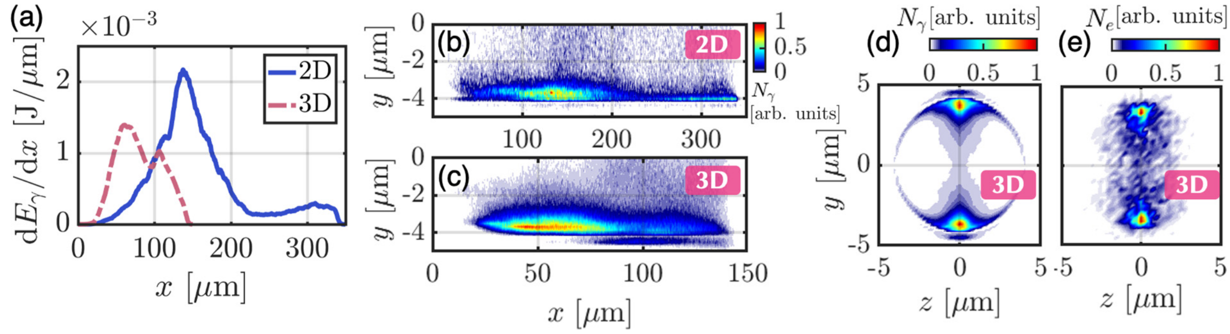

FIG. 5. Photon and electron distribution over space. (a) Photon energy distribution along the x axis. Photon number distribution in (x, y) space for (b) two dimensions and (c) three dimensions. (d) Transverse distribution of photon number in the 3D simulation plotted in (y, z) space. (e) Transverse distribution of the number of high-energy electrons in the 3D simulation plotted in (y, z) space. The considered photons are forward-emitted, accumulated up to 1100 and 500 fs for two and three dimensions, respectively. The photon energy threshold is 100 keV. The energy threshold of the high-energy electrons is 100 MeV.

threshold shown to be critical for photon-photon pair production [31].

Collecting all the forward-emitted photons over the duration of the simulations, Fig. 5 compares the spatial distributions of photons produced in the 2D and 3D simulations. Noting that in the simulations performed here, once a photon is generated, the emission location is marked as the photon location for the duration of the simulation. Corresponding to the electron acceleration, the first peak of emission in three dimensions takes place at $x \sim 60$ μm, well ahead of that in two dimensions, which is located at $x \sim 140$ μm [see Fig. 5(a)]. Up to the first peaks, 38% of laser energy in two dimensions is transferred to particles (photons, electrons, and ions) compared to 41% in three dimensions. Of the transferred energies 0.47% is converted into photons ($\varepsilon_\gamma > 100$ keV) in the 2D simulation in contrast to 0.11% in the 3D simulation. As shown in Eq. (12), η is directly proportional to the electron's relativistic factor, i.e., $\eta \propto \gamma_e$. In the previous section it is noted that the field amplitudes acting on the electrons are similar in both two and three dimensions. Thus the primary cause of the lower conversion rate in three dimensions is due to the lack of electrons at very high energies. Figures 5(b) and 5(c) illustrate the distribution of photons in (x, y) space. The common feature of both distributions is that most photons are generated close to the channel boundary, corresponding to the surfing motion of energetic electrons depicted in Figs. 2(d) and 2(e). The second peak of emission in both simulations becomes weaker in amplitude and accumulates less photon yield following the first peak. The distribution of the emission in the 3D simulation on the transverse plane (y, z) is given in Fig. 5(d). It is clear that the emission is concentrated around the $z = 0$ μm plane with two populated lobes formed near the channel boundaries. Due to the linear polarization of the laser electric field, electrons near $z = 0$ μm where the normal component of E_y fields is the strongest are more susceptible to extraction. Driven by the laser electric field, more electrons travel close to $z = 0$ μm plane [see Fig. 5(e)] and emit photons such that the spatial distribution of produced photons at the moment of the emission is aligned with the direction of laser polarization (in our simulations photons are not allowed to move after their generation).

Figure 6 compares the angular distribution and energy spectrum of 2D and 3D simulations. The photon emission in three dimensions is projected onto a sphere, as illustrated Fig. 6(a). Though the target is cylindrical, the emission pattern does not preserve the same symmetry. From Fig. 6(b), the energy distribution along the azimuthal angle $dE_\gamma/d\theta_\gamma$ demonstrates a divergence of 10° (i.e., the full width at half maximum of the energy distribution curve), which is more than two times wider than that in the polar angle direction. The photon beam in the 2D case is found to be more collimated with a divergence of 6° in $dE_\gamma/d\theta_\gamma$. Distributing emission over θ_γ and photon energy, Figs. 6(c) and 6(d) manifest that the photon beam in two dimensions is better collimated throughout the whole energy spectrum. To further evaluate the quality of the two photon beams, we compare the beam brilliance. The source size of the 3D target is easily decided by its radius while in two dimensions the source size is set as 4×2 μm^2. It is found that the brilliance of γ-ray beams is 2.9×10^{21} and 5.8×10^{20} photons/s mm^2 mrad^2 0.1%BW (at 1 MeV) for two and three dimensions, respectively. Here 0.1%BW means photons are collected within a bandwidth (BW) of 0.1% of the central frequency. In Fig. 6(e) starting from 1.5 MeV, the number of γ-ray photons in two dimensions surpasses that in three dimensions, projecting a larger brilliance in two dimensions for energy level above 1 MeV.

In this section, we compared the photon yield with regard to the simulation dimensionality. Since photon emission is a direct result of electron acceleration, the emission demonstrates correlated features as observed for electrons in Sec. III. The first peak of photon emission in three dimensions arrives early in space due to the high phase velocity. The lack of high-energy electrons makes the conversion of laser energy to γ-ray photons less efficient in three dimensions. Besides the impact on photon number yield, the dimensionality also affects the collimation of the photon beam. With a large divergence angle and a small number of high-energy photons, the 3D γ-ray beam is less bright than the 2D beam.

VI. SUMMARY AND CONCLUSIONS

We have demonstrated the effects of simulation dimensionality on electron acceleration and γ-ray production. There are

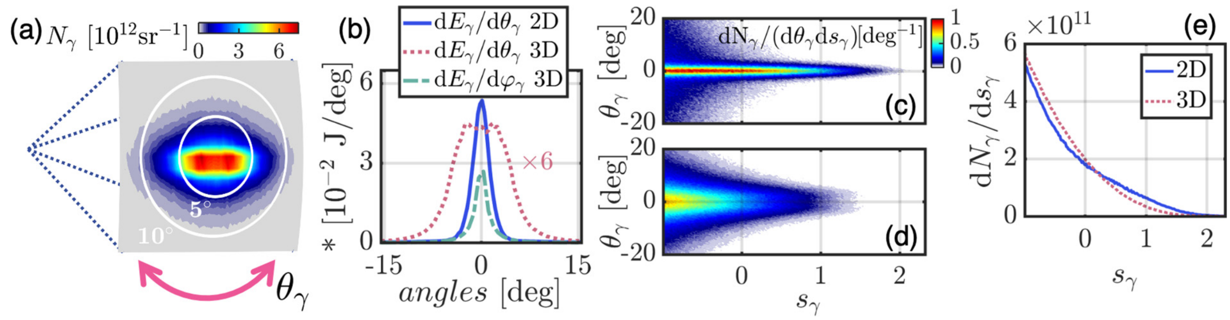

FIG. 6. (a) Photon count per solid angle for the 3D simulation. The solid circles mark polar angles of 5° and 15°. (b) Photon energy distribution over the azimuthal θ_γ and polar angles φ_γ for both two and three dimensions, where $\theta_\gamma = \arctan(p_y/p_x)$ and $\varphi_\gamma = \arctan(p_z/\sqrt{p_x^2 + p_y^2})$. To make the curve for $dE_\gamma/d\theta_\gamma$ of the 3D simulation visible, its y axis is multiplied by a factor of 6. The spectral-angular distribution of the generated γ-ray pulse is shown in the (c) 2D and (d) 3D simulations. Here $s_\gamma \equiv \log_{10}(\varepsilon_\gamma/\text{MeV})$. (e) Photon energy spectra. The considered photons are forward-emitted, accumulated up to 1100 and 500 fs for two and three dimensions, respectively. The photon energy threshold is 100 keV.

significant distinctions between the results obtained in 2D and 3D setups from both analytical consideration and numerical calculation. Though in numerical values v_{ph} is close to the speed of light, the dephasing rate $(v_{\text{ph}}/c - 1)$ which determines the energy gain varies considerably with simulation geometry. The higher dephasing rate observable in the 3D setup terminates the electron acceleration process early in space and time and leads to a reduction of photon emission when compared to two dimensions.

A 2D channel target presents a planar geometry while a 3D target has a cylindrical symmetry. Analytically we have shown that the phase velocity of laser fields propagating inside the targets closely depends on the target geometry; the phase velocity in two dimensions is smaller than that in three dimensions. To be more specific, the dephasing rate in a 2D setup is derived to be 1.5 times slower when controlling for the channel radius and laser wavelength. Through numerical simulations, it is found that the absolute majority of work done on energetic electrons comes from the longitudinal electric field, enabling the investigation of laser-driven particle acceleration based only on one single component of the electric fields. By tracking a fixed segment of laser fields the phase velocity in two dimensions is again shown to be smaller than in three dimensions, matching the correct trend shown in the analytical derivation. It is clear that in 2D simulations electrons surf for a longer period in an accelerating phase compared to 3D simulations. As a result, electrons in two dimensions have an elongated acceleration distance and present a more energetic spectrum, leading to an overestimate of maximum electron energy and the number of high-energy electrons when compared to more realistic 3D simulations.

Similar to electron acceleration, photon emission is strongly impacted by simulation dimensionality. Due to a lack of high-energy electrons, in three dimensions the photon ($\varepsilon_\gamma > 100$ keV) conversion rate is more than four times smaller and the emission falls behind on the generation of energetic photons ($\varepsilon_\gamma > 1.5$ MeV). In three dimensions, the emission is accumulated close to the $z = 0$ plane with a narrow divergence along the polar angle. However, the emission along the azimuthal angle is far more diverged in three dimensions compared to that in a 2D simulation. As a result, the photon beam produced in a 3D setup is found to be less bright. It is also worth noting that the subsequent peaks of photon emission drop sharply in amplitude and duration.

Though 2D numerical simulations are widely applied in the research of laser and microchannel interactions, one should not ignore the overestimate and inaccuracy of results caused by the low phase velocity in 2D simulations. In particular, when carrying out numerical simulations to predict and optimize the output for laser microchannel experiments, it matters to accurately know the exact location of the peaked electron spectrum and therefore 3D simulations are indispensable. We conclude that the 2D simulations are capable of qualitatively reproducing the features of 3D simulations, but for quantitative evaluations and reliable predictions 3D modeling is strongly recommended.

ACKNOWLEDGMENTS

T.W. and A.A. were supported by AFOSR Grant No. FA9550-17-1-0382. D.B. was supported by NSF Grant No. PHY 1903098. K.C. was supported by NSF Grant No. 1821944. Simulations were performed with EPOCH (developed under Engineering and Physical Sciences Research Council Grants No. EPG0549401, No. EPG0551651, and No. EPG0568031) using high-performance computing resources provided by the Texas Advanced Computing Center (TACC) at the University of Texas. This work used the Extreme Science and Engineering Discovery Environment (XSEDE), supported by NSF Grant No. ACI-1548562.

APPENDIX A: E_x FIELD PROFILE

Figure 7 describes the transverse profiles of the peak E_x fields captured at the same snapshot for varied channel width. The lineouts of the E_x field for two and three dimensions at the same channel radius ($R = 4.0$ μm) are very close to each other, but there is already a noticeable deviation from the 3D case when R is reduced to 3.28 μm. In 2D simulations at $R = 2.0$ or 6.0 μm, the amplitude and slope of E_x fields deviate from the 3D case even further.

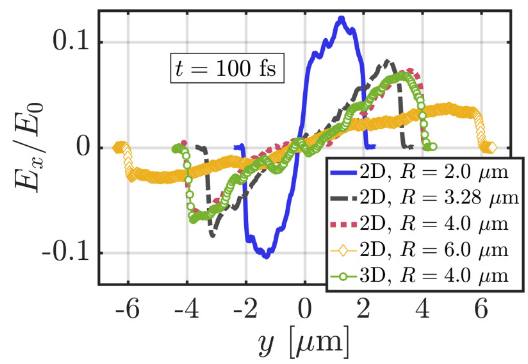

FIG. 7. Peak longitudinal electric field profiles with varied channel width. All the snapshots were taken at $t = 100$ fs.

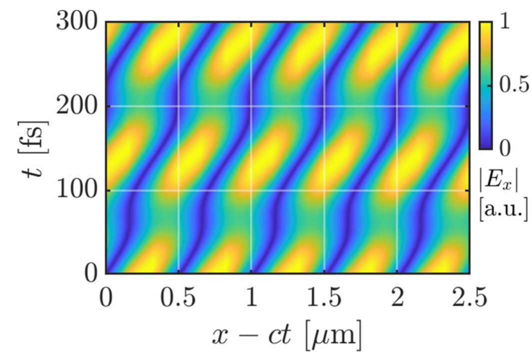

FIG. 8. Temporal profile of E_x fields resulted from the superposition of the first and second waveguide modes. The fields are plotted in a moving window which moves with the speed of light.

APPENDIX B: SUPERPOSITION OF WAVEGUIDE MODES

In Eq. (2), we have chosen the fundamental TM mode ($n = 1$) as the solution of propagating electromagnetic fields in the 2D waveguide. Generally, the dispersion relation of TM modes in the considered setup can be written as $\omega^2/c^2 = k^2 + (n\pi/R)^2$, where $n = 1, 2 \ldots$. Figure 8 shows the temporal profile of $|E_x|$ from the superposition of the first ($n = 1$) and second ($n = 2$) modes, where the ratio between the amplitudes of the first mode and the second mode is 4:1. The superposition of the lowest mode with a higher mode creates the wiggling of the field segments. The phase velocity becomes subluminal for a short time period though the mean phase velocity remains superluminal.

[1] P. P. Rajeev, P. Ayyub, S. Bagchi, and G. R. Kumar, Opt. Lett. **29**, 2662 (2004).
[2] T. Nishikawa, H. Nakano, K. Oguri, N. Uesugi, K. Nishio, and H. Masuda, J. Appl. Phys. **96**, 7537 (2004).
[3] A. Andreev, N. Kumar, K. Platonov, and A. Pukhov, Phys. Plasmas **18**, 103103 (2011).
[4] D. Margarone, O. Klimo, I. J. Kim, J. Prokůpek, J. Limpouch, T. M. Jeong, T. Mocek, J. Pšikal, H. T. Kim, J. Proška, K. H. Nam, L. Štolcová, I. W. Choi, S. K. Lee, J. H. Sung, T. J. Yu, and G. Korn, Phys. Rev. Lett. **109**, 234801 (2012).
[5] M. Blanco, M. T. Flores-Arias, C. Ruiz, and M. Vranic, New J. Phys. **19**, 033004 (2017).
[6] A. Moreau, R. Hollinger, C. Calvi, S. Wang, Y. Wang, M. G. Capeluto, A. Rockwood, A. Curtis, S. Kasdorf, V. N. Shlyaptsev, V. Kaymak, A. Pukhov, and J. J. Rocca, Plasma Phys. Controlled Fusion **62**, 014013 (2019).
[7] S. Vallières, M. Salvadori, A. Permogorov, G. Cantono, K. Svendsen, Z. Chen, S. Sun, F. Consoli, E. d'Humières, C.-G. Wahlström, and P. Antici, Sci. Rep. **11**, 2226 (2021).
[8] N. Naumova, I. Sokolov, J. Nees, A. Maksimchuk, V. Yanovsky, and G. Mourou, Phys. Rev. Lett. **93**, 195003 (2004).
[9] O. Klimo, J. Psikal, J. Limpouch, J. Proska, F. Novotny, T. Ceccotti, V. Floquet, and S. Kawata, New J. Phys. **13**, 053028 (2011).
[10] K. D. Xiao, T. W. Huang, L. B. Ju, R. Li, S. L. Yang, Y. C. Yang, S. Z. Wu, H. Zhang, B. Qiao, S. C. Ruan, C. T. Zhou, and X. T. He, Phys. Rev. E **93**, 043207 (2016).
[11] D. Gozhev, S. Bochkarev, N. Busleev, A. Brantov, S. Kudryashov, A. Savel'ev, and V. Bychenkov, High Energy Density Phys. **37**, 100856 (2020).
[12] B. Feng, L. L. Ji, B. F. Shen, X. S. Geng, Z. Guo, Q. Yu, T. J. Xu, and L. G. Zhang, Phys. Plasmas **25**, 103109 (2018).
[13] S. Jiang, L. L. Ji, H. Audesirk, K. M. George, J. Snyder, A. Krygier, P. Poole, C. Willis, R. Daskalova, E. Chowdhury, N. S. Lewis, D. W. Schumacher, A. Pukhov, R. R. Freeman, and K. U. Akli, Phys. Rev. Lett. **116**, 085002 (2016).
[14] L. Ji, J. Snyder, A. Pukhov, R. Freeman, and K. Akli, Sci. Rep. **6**, 23256 (2016).
[15] D. Stark, T. Toncian, and A. Arefiev, Phys. Rev. Lett. **116**, 185003 (2016).
[16] J. Yu, R. Hu, Z. Gong, A. Ting, Z. Najmudin, D. Wu, H. Lu, W. Ma, and X. Yan, Appl. Phys. Lett. **112**, 204103 (2018).
[17] J. Snyder, L. L. Ji, K. M. George, C. Willis, G. E. Cochran, R. L. Daskalova, A. Handler, T. Rubin, P. L. Poole, D. Nasir, A. Zingale, E. Chowdhury, B. F. Shen, and D. W. Schumacher, Phys. Plasmas **26**, 033110 (2019).
[18] M. Bailly-Grandvaux, D. Kawahito, C. McGuffey, J. Strehlow, B. Edghill, M. S. Wei, N. Alexander, A. Haid, C. Brabetz, V. Bagnoud, R. Hollinger, M. G. Capeluto, J. J. Rocca, and F. N. Beg, Phys. Rev. E **102**, 021201 (2020).
[19] X. Lavocat-Dubuis and J.-P. Matte, Phys. Plasmas **17**, 093105 (2010).
[20] G. Cantono, L. Fedeli, A. Sgattoni, A. Denoeud, L. Chopineau, F. Réau, T. Ceccotti, and A. Macchi, Phys. Rev. Lett. **120**, 264803 (2018).
[21] L. Yi, A. Pukhov, P. Luu-Thanh, and B. Shen, Phys. Rev. Lett. **116**, 115001 (2016).
[22] Z. Lècz and A. Andreev, Phys. Plasmas **24**, 033113 (2017).
[23] D. Rolles, Nat. Photon. **12**, 62 (2018).
[24] W.-M. Wang, Z.-M. Sheng, P. Gibbon, L.-M. Chen, Y.-T. Li, and J. Zhang, Proc. Natl. Acad. Sci. USA **115**, 9911 (2018).
[25] V. Malka, S. Fritzler, E. Lefebvre, E. d'Humières, R. Ferrand, G. Grillon, C. Albaret, S. Meyroneinc, J.-P. Chambaret, A. Antonetti *et al.*, Med. Phys. **31**, 1587 (2004).
[26] L. Robson, P. Simpson, R. J. Clarke, K. W. Ledingham, F. Lindau, O. Lundh, T. McCanny, P. Mora, D. Neely, C.-G. Wahlström *et al.*, Nat. Phys. **3**, 58 (2007).

[27] V. Y. Bychenkov, V. Tikhonchuk, and S. Tolokonnikov, J. Exp. Theor. Phys. **88**, 1137 (1999).

[28] W. Bertozzi, J. A. Caggiano, W. K. Hensley, M. S. Johnson, S. E. Korbly, R. J. Ledoux, D. P. McNabb, E. B. Norman, W. H. Park, and G. A. Warren, Phys. Rev. C **78**, 041601 (2008).

[29] J. Yu, H. Lu, T. Takahashi, R. Hu, Z. Gong, W. Ma, Y. Huang, C. Chen, and X. Yan, Phys. Rev. Lett. **122**, 014802 (2019).

[30] T. Wang and A. Arefiev, Phys. Rev. Lett. **125**, 079501 (2020).

[31] T. Wang, X. Ribeyre, Z. Gong, O. Jansen, E. d'Humières, D. Stutman, T. Toncian, and A. Arefiev, Phys. Rev. Applied **13**, 054024 (2020).

[32] P. P. Rajeev, P. Taneja, P. Ayyub, A. S. Sandhu, and G. R. Kumar, Phys. Rev. Lett. **90**, 115002 (2003).

[33] B. N. Breizman, A. V. Arefiev, and M. V. Fomyts'kyi, Phys. Plasmas **12**, 056706 (2005).

[34] T. Wang, Z. Gong, K. Chin, and A. Arefiev, Plasma Phys. Control. Fusion **61**, 084004 (2019).

[35] D. B. Zou, A. Pukhov, L. Q. Yi, H. B. Zhuo, T. P. Yu, Y. Yin, and F. Q. Shao, Sci. Rep. **7**, 42666 (2017).

[36] Z. Gong, A. Robinson, X. Yan, and A. Arefiev, Plasma Phys. Control. Fusion **61**, 035012 (2019).

[37] S. Jiang, A. G. Krygier, D. W. Schumacher, K. U. Akli, and R. R. Freeman, Phys. Rev. E **89**, 013106 (2014).

[38] D. A. Serebryakov, T. M. Volkova, E. N. Nerush, and I. Y. Kostyukov, Plasma Phys. Controlled Fusion **61**, 074007 (2019).

[39] D. J. Stark, L. Yin, B. J. Albright, and F. Guo, Phys. Plasmas **24**, 053103 (2017).

[40] J.-L. Liu, M. Chen, J. Zheng, Z.-M. Sheng, and C.-S. Liu, Phys. Plasmas **20**, 063107 (2013).

[41] K. D. Xiao, C. T. Zhou, K. Jiang, Y. C. Yang, R. Li, H. Zhang, B. Qiao, T. W. Huang, J. M. Cao, T. X. Cai, M. Y. Yu, S. C. Ruan, and X. T. He, Phys. Plasmas **25**, 023103 (2018).

[42] A. Robinson, A. Arefiev, and V. Khudik, Phys. Plasmas **22**, 083114 (2015).

[43] T. Arber, K. Bennett, C. Brady, A. Lawrence-Douglas, M. Ramsay, N. Sircombe, P. Gillies, R. Evans, H. Schmitz, A. Bell *et al.*, Plasma Phys. Control. Fusion **57**, 113001 (2015).

[44] A. Arefiev, D. J. Stark, T. Toncian, and M. Murakami, Phys. Plasmas **27**, 063106 (2020).

[45] A. Pukhov, CERN Yellow Reports **1**, 181 (2016).

[46] L. Landau and E. Lifshitz, *The Classical Theory of Fields* (Butterworth-Heinemann, Oxford, 1987), Chap. 9.